

# Optical Engineering

[SPIDigitalLibrary.org/oe](http://SPIDigitalLibrary.org/oe)

## **Temperature dynamics of aluminized cyclotrimethylenetrinitramine fireballs for event classification**

J. Motos Gordon  
Kevin C. Gross  
Glen P. Perram



**SPIE**

# Temperature dynamics of aluminized cyclotrimethylenetrinitramine fireballs for event classification

J. Motos Gordon

Kevin C. Gross

Glen P. Perram

Air Force Institute of Technology  
Department of Engineering Physics  
2950 Hobson Way  
Wright-Patterson Air Force Base  
Dayton, Ohio 45433  
E-mail: [glen.perram@afit.edu](mailto:glen.perram@afit.edu)

**Abstract.** The remote sensing and classification of battlespace explosions might be improved by developing optical signatures for the heat released during secondary combustion. To explore this possibility, mid-wave infrared spectra ( $1800$  to  $10,000\text{ cm}^{-1}$ ) from the detonation of aluminized cyclotrimethylenetrinitramine (RDX) have been observed and analyzed. The field detonations of 12 high-explosive compositions of RDX with varying aluminum and liner volumes were remotely observed with a suite of imagers, spectrometers, and radiometers. The evolution of spatially averaged fireball temperatures has been estimated from the infrared spectra. The effective temperatures decay from initial values of  $1290$  to  $1850\text{ K}$  to less than  $1000\text{ K}$  during a  $1\text{-s}$  interval. Secondary maxima are observed in the temperature profiles, indicating delayed combustion resulting from the mixing of atmospheric oxygen with the detonation products. The heat released in the secondary combustion is well correlated with the high explosive and liner theoretical heats of secondary combustion and exhibits an average efficiency of about  $50\%$ . Fireball lofting rates increase by more than  $50\%$  for events where the combustion heat release increases by a factor of  $2$ . © 2014 Society of Photo-Optical Instrumentation Engineers (SPIE) [DOI: [10.1117/1.OE.53.2.021106](https://doi.org/10.1117/1.OE.53.2.021106)]

Subject terms: fireball temperature; postdetonation combustion; classification; aluminized; liners.

Paper 130433SSP received Mar. 19, 2013; revised manuscript received Aug. 8, 2013; accepted for publication Sep. 24, 2013; published online Oct. 25, 2013.

## 1 Introduction

Optical forensics of explosive events is important for both battlespace characterization and civilian safety. Classification of high-explosive material, weight, and device type from remotely sensed, spectral, and temporal signatures with or without imagery, has been elusive. Recently, we have developed methods with limited ability to differentiate between trinitrotoluene (TNT)-based and enhanced novel explosives, cased versus uncased detonations, and air-dropped versus static detonations.<sup>1–7</sup> In particular, the hydrogen-to-carbon stoichiometry in the high explosive (HE) can be estimated from spectrally resolved  $\text{CO}$ ,  $\text{CO}_2$ , and  $\text{H}_2\text{O}$  emission in the mid-infrared.<sup>2,6</sup> Simple radiative transfer and chemical kinetic models were employed to reduce the dimensionality of the extracted classification features and to improve the independence of the observed signatures, while retaining physically interpretable parameters. These physical constraints are keys to the pattern-recognition algorithms.

Empirical features extracted from field observations without physical modeling have not been successful in event classification. High-dimensional fireball models, including the complex interplay of chemical kinetics, radiative transfer, and fluid dynamics, while critical to munitions design and development, have also been unproductive for event classification. Detailed physical models of detonation fireballs involve many independent variables, whereas the dimensionality of remotely sensed data is often low. For these conditions, the stability of feature saliency and classification can

be significantly degraded when employing high-dimensional modeling.

In the present work, we seek to exploit the temporal dependence of an effective fireball temperature to infer the relative heat released during secondary combustion. Such information may be useful in inferring high-explosive weight and improving classification based on the spectrally derived stoichiometry alone. Unfortunately, peak fireball temperatures and total emission intensities are highly variable even within an explosive class and yield minimal information regarding device weight.<sup>1,4</sup> Our strategy is to separate the radiatively cooled decay of the initial detonation temperature from the increased temperature observed during secondary combustion. By varying the amount of aluminum in a cyclotrimethylenetrinitramine (RDX) HE, both the amount of energy released and the temporal delay due to atmospheric mixing with detonation products are likely affected. The presence of aluminum is desired due to its large heat release during oxidation reactions.<sup>8</sup> The presence of an oxide layer around the aluminum as well as the particle size strongly influences explosion and combustion mechanisms.<sup>9–18</sup> Carney et al.<sup>9</sup> suggest that aluminum acts as an additional fuel in the explosion reaction beyond the detonation and that its oxide transients react favorably with detonation products, especially when external atmospheric oxygen is present. Work by Lefrancois et al.<sup>15</sup> on the effect of nanometric aluminum additives to HEs indicates that Al particles of diameter greater than  $100\text{ nm}$  do not contribute to ballistics performance. Performance benefits of aluminum may lie in timescales exceeding  $1\text{ ms}$ , well beyond the detonation.<sup>9,19</sup> We do not intend to study aluminum kinetics directly, but

rather attempt to correlate field observations with varying combustion heat release.

Previous experimental works have extracted the temporal temperature profiles of open-air field explosions.<sup>5,6,20–26</sup> Recent work by Wilkinson et al.<sup>8</sup> and Lewis and Rumchik<sup>24</sup> have also noted postdetonation temperature trends using emission spectroscopy from chamber detonations of 20- to 40-g samples of octogen (HMX,  $C_4H_8N_8O_8$ ) and cyclotrimethylenetrinitramine (RDX,  $C_3H_6N_6O_6$ ). Optical pyrometry has also been used to study both chamber<sup>9</sup> and open-air detonations of TNT ( $C_7H_5N_3O_6$ ) and metalized nitromethane (NM,  $CH_3NO_2$ ).<sup>25,26</sup> In the present work, we use an infrared Fourier-transform spectrometer (FTS) with a temporal resolution of 12 to 18 ms to observe field detonations of aluminized RDX. While the instrument is unable to resolve the initial detonation, the FTS adequately samples the subsequent fireball resulting from secondary combustion of detonation products with atmospheric oxygen. This postdetonation combustion fireball evolves over a 0.5- to 1-s timescale, and our observation that scene-change artifacts are negligible in these measured spectra is consistent with numerical simulations of FTS observations of evolving fireballs.<sup>27</sup> We recently reported on the shock dynamics for the same events using high-speed visible imagery.<sup>28–30</sup> Initial Mach numbers of 4.7 to 8.2 were observed, a factor of 3 to 4 slower than the theoretical maximum. Shocks detach from the fireball at 1.9 to 3.4 ms after detonation. The fireballs attain maximum radii of 4.3 to 5.8 m at 30 to 50 ms with a stable area until 150 to 200 ms. At  $t > 300$  ms, the fireball begins to loft due to buoyancy. The fireballs are sooty and optically thick, and the emissivity–area product obtained

from mid-IR spectra agree with the visible fireball imagery to within 12%.

## 2 Experimental Setup and Explosive Materials

A set of 22 novel aluminized munitions was detonated at a Department of Defense test site in Florida. Details of the test site have been reported previously.<sup>28–30</sup> The test items are 16-in. (0.41-m) tall mild steel tubes with 0.5-in. (0.013-m) thick walls and a 7-in. (0.18-m) inner diameter. The steel tubes are lined with an aluminized polyethylene (PE) annulus in the inner diameter and filled with melt-cast RDX-based HE with varying amounts of aluminum and paraffin wax binder. The test items are detonated 1.25 m above ground level atop a sacrificial wooden test stand. Table 1 specifies the amount of material present in the test items. The events in Table 1 and subsequent tables in this article are listed from least to most total number of moles in the test articles. The event nomenclature,  $E$ , denotes chronological order in the test sequence. Paraffin wax in the HE and PE in the liner are used as reasonable surrogates for the actual binders.

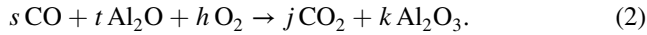
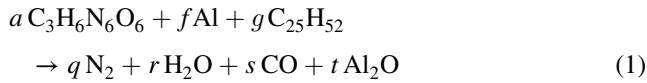
In order to reasonably estimate stoichiometric quantities of the detonation products for the secondary combustion phase, it was hypothesized that due to the geometry of the liner, only the HE completely participates in the detonation and explosion reaction and that the liner is fragmented but only partially participates in the explosion phase. The liner does, however, fully participate in the combustion phase of the fireball. This is not an unreasonable hypothesis, as the analysis of high-speed visible imagery presented in our previous article<sup>29</sup> suggests that the energy transferred to the shock wave of the explosion constitutes only about 2% to

**Table 1** Composition of test articles.

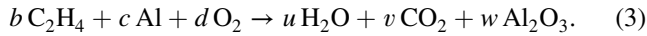
Event	Moles of material							Total
	RDX	A1HE	Wax	HE total	PE	Al liner	Liner total	
E8	59.19	0.00	7.64	66.83	0.00	0.00	0.00	66.83
E13	48.77	33.19	7.69	89.65	0.00	0.00	0.00	89.65
E5	49.02	29.54	8.09	86.65	0.00	0.00	0.00	86.65
E16	47.38	0.00	6.12	53.50	31.75	26.25	58.00	111.50
E7	47.30	0.00	6.11	53.41	44.71	15.04	59.75	113.16
E9	39.17	23.62	6.46	69.25	31.75	26.25	58.00	127.25
F4	39.29	23.71	6.48	69.48	44.71	15.04	59.75	129.23
E17	39.15	23.62	6.46	69.23	44.71	15.04	59.75	128.97
E11	32.49	8.59	4.72	45.79	77.92	39.73	117.65	163.44
E1	23.80	0.00	3.08	26.88	95.09	78.34	173.43	200.32
E6	19.76	11.92	3.26	34.94	95.09	78.34	173.43	208.37
E3	23.60	0.00	3.05	26.65	133.81	44.93	178.74	205.39

15% of the expected RDX heat of detonation, assuming a constant release of energy.

Following Cooper's<sup>31</sup> reaction-product hierarchy rules of thumb, the detonation and secondary combustion stoichiometries for the composite RDX-Al-wax HE are



The corresponding stoichiometry for the PE-Al liner secondary combustion is



The heat capacity, heat of detonation, and heat of combustion for each event are computed using the reaction stoichiometry and NIST-JANNAF Thermochemical Table<sup>32</sup> at 1300 K and are summarized in Table 2. The combustion product heat capacities,  $C_{p,c}$ , increase even as the amount of RDX in Table 1 decreases for each respective event. This is because the overall total number of moles increases as more PE-Al liner material is taken into account in the combustion stoichiometry. The displacement of a proportionate amount of HE as the liner volume increases also explains the trends in the heats of detonation and combustion in Table 2.

The instrumentation suite consists of a 82-Hz FTS, 100-kHz four-band radiometer, high-speed digital camera operating at 3000 to 4200 fps, and a standard witness audio-visual digital camera. Signatures are collected from an

unobstructed standoff distance of 335 m. FTS signatures are the primary dataset used for the analysis in this work. The FTS was fitted with a 75-mrad telescope giving a 25-m diameter field-of-view (FOV) at the target. Bore-sighted video indicated that fireballs at peak area occupied only about 15% of the FOV and had a dwell time of about 1 s before ascending or migrating out of the FOV due to wind gusts. Meteorological conditions were recorded prior to each detonation event throughout the 2-week data collection phase.<sup>30</sup> Of the 22 scheduled detonations, only 13 high-speed digital camera signatures were successfully collected and only 12 of those 13 detonation events netted useable FTS spectra.

The ABB-Bomem MR-254 FTS operated at 82 Hz with a spectral resolution of  $16 \text{ cm}^{-1}$  ( $\Delta\tilde{\nu} = 7.71 \text{ cm}^{-1}$ ) using InSb (1800 to 10,000  $\text{cm}^{-1}$ ) and InGaAs (5600 to 10,000  $\text{cm}^{-1}$ ) detectors. Some interferograms were collected at  $8 \text{ cm}^{-1}$  resolution at a rate of 56 Hz. The interferograms were over-sampled at half-HeNe wavelengths, putting the Nyquist frequency at  $15,802 \text{ cm}^{-1}$ . This is well beyond the response of InSb and InGaAs detectors, and thus sufficiently avoiding aliasing of the signal reconstruction during Fourier transformation. Only the mid-infrared spectra from the InSb detector are reported in the current work. The majority of the InGaAs spectral range overlaps and agrees with the short wavelength limit of the InSb detector.

The FTS was calibrated in the field following a method detailed by Gordon et al.<sup>28,30</sup> and Gross.<sup>2</sup> A low-temperature (283 to 353 K) wide-area blackbody (BB) source and a high-temperature (1523 K) cavity BB source were used to calibrate the FTS detector. The wide-area BB was positioned a few centimeters from the FTS entrance aperture and over-filled the FOV, and established the spectral instrument

**Table 2** Thermodynamic properties of test articles.

Event	Heat capacity		Heat of combustion, $\Delta H_c$				Detonation, $\Delta H_d$		Theoretical $T_0$
	$C_{p,c}$ (J/K)	$C_{p,d}$ (J/K)	RDX (kJ)	HE (kJ)	Liner (kJ)	Total (kJ)	RDX (kJ)	HE (kJ)	$\Delta H_{d,\text{RDX}}/C_{p,d}$ (K)
E8	21.06	31.66	49.97	103.72	0.00	103.72	74.03	138.14	2338
E13	21.50	29.55	41.17	120.29	0.00	120.29	60.99	126.60	2064
E5	21.88	30.21	41.38	120.56	0.00	120.56	61.30	130.54	2029
E16	25.05	29.51	40.00	83.06	64.27	147.33	59.26	110.62	2008
E7	26.94	30.46	39.93	82.90	71.98	154.87	59.19	110.40	1943
E9	25.65	28.28	33.06	96.28	64.27	160.55	48.98	104.21	1732
E4	27.64	29.37	33.17	96.63	71.98	168.60	49.14	104.59	1673
E17	27.57	29.28	33.05	96.26	71.98	168.24	48.96	104.19	1672
E11	31.35	27.98	27.42	67.07	136.86	203.93	40.63	80.60	1452
E1	32.98	25.19	20.09	41.76	192.26	234.02	29.77	55.61	1182
E6	33.31	24.62	16.68	48.59	192.26	240.85	24.71	52.60	1004
E3	38.64	28.08	19.92	41.41	215.35	256.75	29.51	55.14	1051

response (gain) and self-emission (offset) between 1750 and 3000  $\text{cm}^{-1}$  via standard calibration methods.<sup>33</sup> Since instrument self-emission becomes negligible beyond 2500  $\text{cm}^{-1}$ , the high-temperature cavity BB measurements enable the determination of the relative instrument gain beyond 3000  $\text{cm}^{-1}$ . An absolute scale for the relative gain curve between 3000 and 10,000  $\text{cm}^{-1}$  was established by comparison with the gain curve previously found using the low-temperature BB source where they overlap between 2500 and 3000  $\text{cm}^{-1}$ .

### 3 Results

#### 3.1 Spectra

The infrared spectrum for event E9, with a temporal resolution of 12.1 ms, is illustrated in Fig. 1(a). A broadband emission, attenuated by the atmosphere, initially increases as the fireball grows and temperature increases. The subsequent decay is relatively long lived,  $> 1$  s, and depends on spectral component. For example, the emission from  $\text{CO}_2$  near 2360  $\text{cm}^{-1}$  decays more slowly than the broader continuum. The 16- $\text{cm}^{-1}$

resolution of the single spectrum at 0.28 s after detonation in Fig. 1(b) is sufficient to discern gas phase emission from  $\text{CO}_2$  and  $\text{H}_2\text{O}$  from the gray-body (soot) signal, even in the presence of significant atmospheric attenuation. There are approximately 2126 spectral samples illustrated as individual data points. The observed spectra represent a spatial average over the full fireball area with a spectrally varying optical depth into the fireball. This average is weighted to higher temperature (more emissive) regions and largely limited to a layer near the surface. In previous spectral observations of uncased, well-engineered munitions, we observed a smaller contribution from broadband emission, particularly at longer times, when soot particulates have been consumed.<sup>2,6</sup> The current aluminized explosives retain a significant broadband component to the spectra throughout the secondary combustion.

A low-dimensionality radiative transfer model has previously been developed<sup>2</sup> to describe the fireball's source radiance. The purpose of this model is to extract a few key, physically based features, for pattern recognition rather than exploring the complex interplay of chemical kinetics, radiative transfer, and fluid dynamics. Assuming

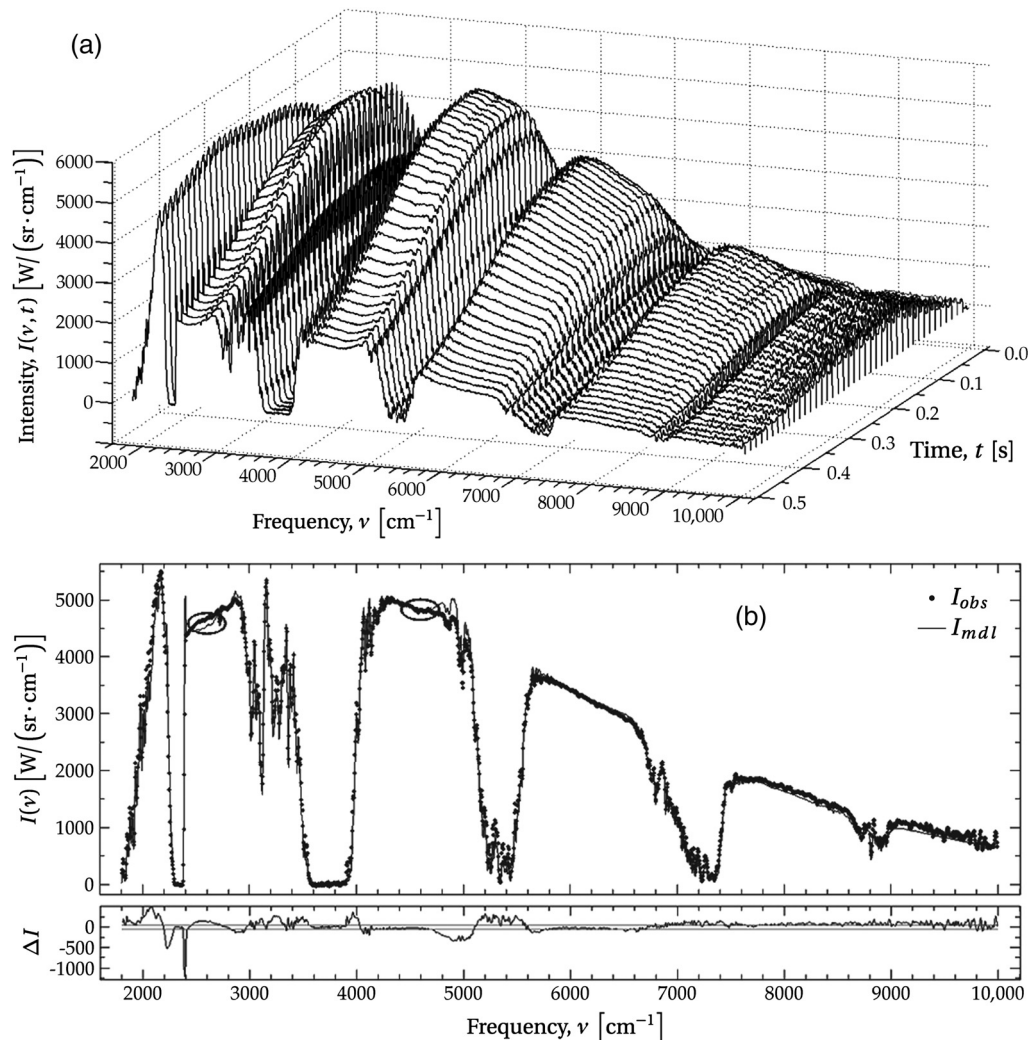


**Fig. 1** (a) Temporally resolved spectra for event E9 and (b) the Fourier-transform spectrometer (FTS)-observed spectral intensity of event E9 at 0.28 s after detonation. Two spectral regions: 2500 to 2700 and 4500 to 4700  $\text{cm}^{-1}$  of continuum radiation are indicated for the two-color temperature determination. A fit of the observed spectra to the radiative transfer model of Eq. (4) yields fit residuals of  $\sim 3.7\%$ , except in the vicinity of the  $\text{CO}_2$  4.3- $\mu\text{m}$  band.



a homogeneous fireball in local thermodynamic equilibrium, negligible effects of scattering, and a large standoff distance, the apparent source radiance can be approximated as

$$I(v) = \tau_{\text{atm}}(v) r^2 \varepsilon(v) B(v; T), \quad (4)$$

where  $B(v; T)$  is the Planckian distribution at effective temperature ( $T$ ),  $r^2$  (A) is the fireball projected area,  $\tau_{\text{atm}}$  is the atmospheric transmission, and  $\varepsilon(v)$  is the source emissivity.

Absorption cross-sections,  $\sigma_i$ , for  $\text{H}_2\text{O}$ ,  $\text{CO}_2$ , and  $\text{CO}$  at  $T = 275$  to  $3000$  K are obtained from the HITRAN database<sup>34</sup> to express emissivity as

$$\varepsilon(v) = 1 - \exp[-r(\kappa_p + \sum \xi_i \sigma_i(v; T))], \quad (5)$$

where  $\kappa_p$  is the particulate absorption coefficient, and  $\xi_i$  is the molecular concentration of specie  $i$ .

The Boltzmann factor is included in the definition of the absorption cross-section.<sup>2</sup> The radiative transfer spectral model is realized by multiplying the source spectrum by the atmospheric transmittance and convolving it with the FTS instrument line shape. The state of the atmosphere and weather conditions have been previously reported.<sup>30</sup>

The radiative transfer model of Eqs. (4) and (5) neglects a number of important phenomena with the goal of extracting via nonlinear regression a unique, minimum set of physically constrained signatures for the purpose of pattern recognition and event classification. For example, soot's contribution to emissivity via  $\kappa_p$  is assumed to be wavelength independent (i.e., gray) but can exhibit a substantial spectral variation across the mid-IR,<sup>35</sup> particularly when optically thin conditions prevail. At a soot volume fraction  $f_v = 10^{-3}$  and 500-cm optical path, the parametric expressions<sup>36</sup> for the complex index of refraction of hydrocarbon soot predict emissivity values that monotonically increase from  $\sim 0.4$  to  $\sim 0.9$  between  $1800$  and  $10,000$   $\text{cm}^{-1}$ . Neglecting this substantial wavelength dependence could bias the spectrally retrieved temperature by more than  $200$  K. A 10-fold increase in  $f_v$  increases the minimum soot emissivity to  $0.99$ , rendering the fireball opaque.

The model is also limited by assuming a single temperature adequately represents both the broadband emission and the ro-vibrational distribution within the molecular spectra. The probability per collision for vibrational relaxation of  $\text{CO}$  at elevated temperatures is about  $10^{-3}$ , yielding rapid rates at atmospheric pressure for single vibrational quanta transfer to translation and relaxation time scales of  $\sim 1$   $\mu\text{s}$ .<sup>37</sup> However, the non-Boltzmann, Treanor distribution for vibrational populations in  $\text{CO}$  resulting from vibrational-to-vibrational energy transfer have been observed for optical and electron excitations in  $\text{N}_2$  and  $\text{O}_2$ , even at pressures exceeding  $1$  atm.<sup>38</sup> Furthermore, the weighting of various regions within the fireball due to turbulent mixing of the atmosphere might significantly bias extracted temperatures to higher than the spatial average. Despite these limitations, the low-parameter model with a single effective temperature captures much of the variation in the observed spectra throughout the evolution of the postdetonation combustion fireball.

Optical depth is included in the spectral model, but with a length scale that is the same as the fireball size. The model does not allow for temperature or specie concentration variations inside the fireball. This is a single-layer,

single-temperature model which matches the spectral signatures with  $\sim 3\%$  average residual, as discussed below. There are effects in the observed spectra associated with optical thickness that are not captured. However, these differences are greater for muzzle flashes<sup>39</sup> than for detonation fireballs<sup>2,6</sup> and are minimized for the current sooty events.

A fit of Eq. (2) to the spectrum is provided in Fig. 1(b), establishing a best estimate for the model parameters:  $T = 1800 \pm 3.3$  K,  $r = 4.7 \pm 0.04$  m,  $\xi_{\text{CO}_2} = 4.36 \pm 0.9 \times 10^{17} \text{ cm}^{-3}$ ,  $\xi_{\text{H}_2\text{O}} = 6.20 \pm 0.6 \times 10^{17} \text{ cm}^{-3}$ , and  $\kappa_p = 1.33 \pm 0.03 \times 10^{-3} \text{ cm}^{-1}$ . The fireball radius extracted from the infrared spectrum compares favorably with the size previously determined from high-speed visible imagery of  $R = 5.1 \pm 0.4$  m.<sup>28–30</sup> The uncertainties reported for these parameters reflect only the statistical fit errors. The systematic errors associated with the simplified model surely dominate. As previously mentioned, ignoring spectral variations in soot emissivity could bias temperatures by  $\sim 200$  K. The model does match the observations moderately well with a median relative error of  $3.7\%$ . Figure 1(b) illustrates the spectrally dependent residuals with the largest differences occurring at the sharp, blue edge of the atmospheric  $\text{CO}_2$  absorption band near  $2325 \text{ cm}^{-1}$  ( $4.3 \mu\text{m}$ ). The full temporal dependence of the fireball temperature estimated from these spectral simulations for several events is provided in Fig. 2.

For the present work, the spectral simulations are not necessary for an estimate of the temperatures. Figure 1(b) highlights two bands in the continuum region (Band1 =  $2500$  to  $2700 \text{ cm}^{-1}$  and Band2 =  $4500$  to  $4700 \text{ cm}^{-1}$ ) of the measured spectrum where spectral intensities are compared with a theoretical Planckian distribution to determine the two-color temperature. These two continuum region bands are chosen because they are both outside the atmospheric absorption bands as well as the emission bands from fireball plume and atmospheric constituents such as  $\text{H}_2\text{O}$  and  $\text{CO}_2$ . The resulting temperature profiles,  $T(t)$ , derived from both the spectral simulation and the two-band pyrometry, are depicted in Fig. 2. The chosen intensity ratio exhibits a nearly linear dependence of temperature in the range  $T = 800$  to  $1900$  K. The ratio of the FTS-measured intensities in Fig. 1(b) is  $1.0313 \pm 0.005$  corresponding to a temperature of  $1828 \pm 9.1$  K.

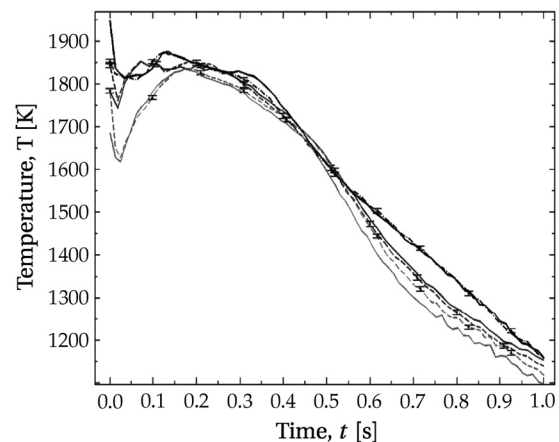


**Fig. 2** Comparison of temperature profiles from the spectral model of Eq. (4) shown as dashed lines and the two-color Planckian method, shown as solid lines, for events: E9 shown in black, E4 shown as dark grey, and E17 shown as light grey.

Recall that the RDX-based HEs in the present work are under-oxidized. Upon detonation, heated carbonaceous soot and other particulates undergo further oxidation reactions in the turbulent fireball. However, the concentrations of these particulates appear to decay slowly enough in the 1-s time-window after detonation, so that an assumption of gray-body emissions from the fireball is still applicable. This notion seems to be validated by comparison of the temperature profiles in Fig. 2, where the two-color best-fit Planckian profile closely trends with the spectral model-derived temperature profile. Because of this slow decay, the measured spectra sufficiently exhibit gray-body behavior, and thus allow a valid means for comparison of measured spectral intensity ratios with calculated theoretical Planckian intensity ratios. The FTS temporal resolution of 12 ms is not fine enough to allow monitoring of the extremely rapid temperature rise immediately after detonation.

### 3.2 Temperature Dynamics

The dynamics of the fireball temperature are dictated by: (1) a sudden initial temperature rise given by the energy released from the detonation into heating, (2) rapid expansion of the fireball, (3) radiative cooling, (4) turbulent mixing of the cooler atmosphere with the detonation by-products, and (5) secondary combustion of detonation by-products with atmospheric oxygen. A thorough analysis of these processes does not lead to the extraction of key features for classification. Our approach involves separating the heat released during secondary combustion from the initial radiative cooling. In the final analysis, only the area under the  $T(t)$  curve, above the radiatively cooled initial temperature, is relevant to the estimation of heat of combustion. Thus, we chose a global, empirical model for the fireball temperature

$$\frac{dT}{dt} = -a(T^4 - T_{\text{atm}}^4) + b(e^{-ct} - e^{-dt}). \quad (6)$$

The initial temperature,  $T_o$ , should be proportional to the heat of detonation,  $\Delta H_d$ , relative to the total heat capacity for the detonation products,  $C_{p,d}$ . The Stefan–Boltzmann law describes the radiative cooling with

$$a = \frac{(\varepsilon A)\sigma_{\text{SB}}}{C_{p,c}}, \quad (7)$$

and  $\sigma_{\text{SB}} = 5.67 \times 10^{-8} \text{ Wm}^{-2} \text{ K}^{-4}$ . The ambient temperature is low and may be neglected in the first term on the right side of Eq. (2). Radiative cooling dominates only at the earliest times when the temperature is high and turbulent mixing has not fully developed. The HE is under-oxidized, and the second term in Eq. (2) represents the combustion of detonation products upon mixing with atmospheric oxygen reduced by the mixing with cooler air. We employ the heat capacity of the combustion products,  $C_{p,c}$ , to describe the temperature evolution.

The release of the heat of combustion,  $\Delta H_c$ , is not rapid, and the first exponential term in Eq. (2) accounts for the rate of turbulent mixing. As the detonation products are fully consumed, no additional heat is released and the second exponential represents this decay of combustion reagent concentration. The total heat released during secondary combustion is obtained from the time integral of the second

term in Eq. (2) and should be proportional to the heat of combustion:

$$\Delta H_c \propto C_{p,c} \int_0^\infty b(e^{-ct} - e^{-dt})dt = b\left(\frac{1}{c} - \frac{1}{d}\right)C_{p,c}. \quad (8)$$

The full temperature rise from the heat of combustion is not realized due to convective cooling and incomplete combustion, and the fit parameter  $b$  allows for a reduced effect. Further justification for the use of the empirical Eq. (2) is provided in the following discussion of the experimental results.

An example fit of the numerical solution to Eq. (2) for the temperatures extracted for event E9 is illustrated in Fig. 3. The resulting fit parameters  $T_o$ ,  $a$ ,  $b$ ,  $c$ ,  $d$ , and their associated uncertainties for each event are reported in Table 3.

The observed initial temperatures,  $T_o = 1290$  to  $1848 \text{ K}$ , do not correlate well with the composite HE heat of detonation, as illustrated in Fig. 4. The spectrometer scans rather slowly, 82 Hz, relative to the detonation, and the peak temperature is not accurately observed. Thus, the empirical initial temperature,  $T_o$  is not a good parameter for event classification. As reported in our previous study,<sup>29,30</sup> the efficiency of converting the heat of detonation into the shock front decreases with increased aluminum and liner content. It is not surprising that the observed initial temperatures are about 30% to 85% of the HE detonation energy predictions.

The magnitude of the radiative cooling parameter,  $a = 4.6$  to  $8.5 \times 10^{-10} \text{ s}^{-1} \text{ K}^{-3}$ , is consistent with the fireball size and heat capacity. For a BB ( $\varepsilon = 1$ ) and a typical fireball area ( $A \approx 333 \text{ m}^2$ ), and the combustion product heat capacities of Table 2, Eq. (2) predicts that the radiative cooling is described by  $a = 4.9$  to  $9.0 \times 10^{-10} \text{ s}^{-1} \text{ K}^{-3}$ , depending on the event heat capacity. Thus, it is estimated that time scale for the initial temperature decay is  $aT_o^3 = 1.93$  to  $4.77 \text{ s}^{-1}$ . Despite being in the same range of values, there is no clear correlation between the model fit parameter-derived  $a$  and calculated  $a$  values.

A strong correlation,  $r = 0.96$ , is observed between the secondary combustion fit parameters,  $b$ ,  $c$ , and  $d$ , and the thermodynamic properties,  $\Delta H_c$  and  $C_{p,c}$ , as shown in

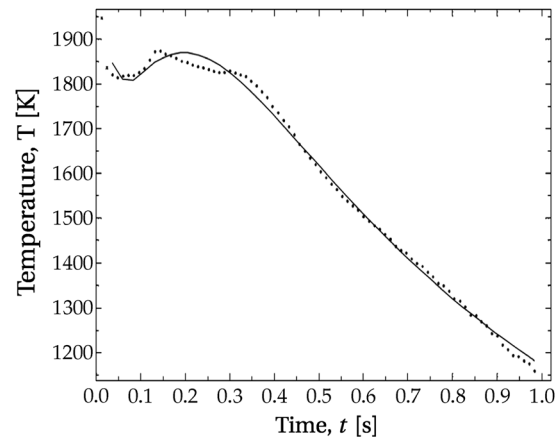


**Fig. 3** Temperature profile observed for event E9 and fit of the numerical solution to Eq. (6), yielding the fit parameters provided in Table 3.

**Table 3** Fit parameters for numerical solution to Eq. (6).

Event	ODE empirical model				
	$T_0$ (K)	$a$ ( $\times 10^{-10} \text{ s}^{-1} \text{ K}^{-3}$ )	$b$ ( $\times 10^4 \text{ K s}^{-1}$ )	$c$ ( $\text{s}^{-1}$ )	$d$ ( $\text{s}^{-1}$ )
E8	$1290.4 \pm 34.5$	$8.01 \pm 0.9$	$2.40 \pm 0.7$	$6.25 \pm 0.0003$	$13.85 \pm 3.0$
E13	$1758.1 \pm 13.8$	$5.65 \pm 0.6$	$3.93 \pm 0.9$	$4.74 \pm 0.0001$	$7.55 \pm 0.6$
E5	$1723.6 \pm 53.2$	$5.66 \pm 0.8$	$1.52 \pm 0.4$	$5.26 \pm 0.0003$	$18.33 \pm 6.1$
E16	$1631.4 \pm 22.5$	$8.53 \pm 1.1$	$8.40 \pm 1.0$	$7.21 \pm 0.5826$	$9.62 \pm 0.2$
E7	$1489.5 \pm 32.8$	$7.46 \pm 1.1$	$1.00 \pm 0.2$	$3.24 \pm 0.0001$	$18.64 \pm 5.0$
F.9	$1848.3 \pm 18.3$	$5.08 \pm 0.3$	$2.04 \pm 0.4$	$4.21 \pm 0.4088$	$10.32 \pm 1.6$
E4	$1813.4 \pm 36.7$	$5.08 \pm 1.0$	$2.91 \pm 1.3$	$4.86 \pm 0.0002$	$9.09 \pm 1.8$
E17	$1673.7 \pm 29.4$	$5.80 \pm 1.2$	$8.11 \pm 6.9$	$6.08 \pm 0.0002$	$7.80 \pm 1.4$
E11	$1685.1 \pm 62.4$	$5.90 \pm 1.7$	$1.28 \pm 0.6$	$3.65 \pm 0.0002$	$13.56 \pm 5.5$
E1	$1603.7 \pm 40.9$	$7.47 \pm 1.5$	$2.63 \pm 1.2$	$5.29 \pm 0.0013$	$14.70 \pm 11.7$
E6	$1805.1 \pm 27.3$	$4.62 \pm 0.8$	$3.97 \pm 1.5$	$5.05 \pm 0.0001$	$9.03 \pm 1.4$
E3	$1648.4 \pm 35.6$	$7.07 \pm 1.7$	$2.75 \pm 1.2$	$4.51 \pm 0.0002$	$9.96 \pm 2.1$

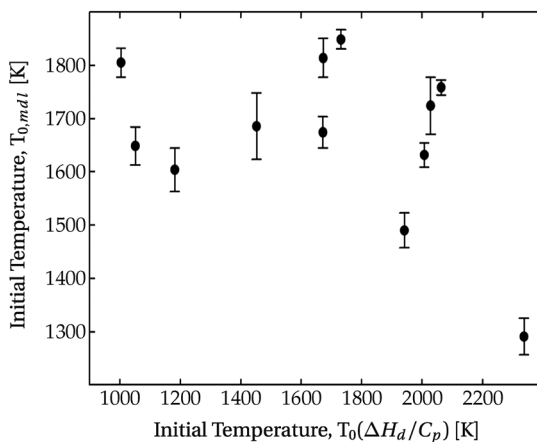
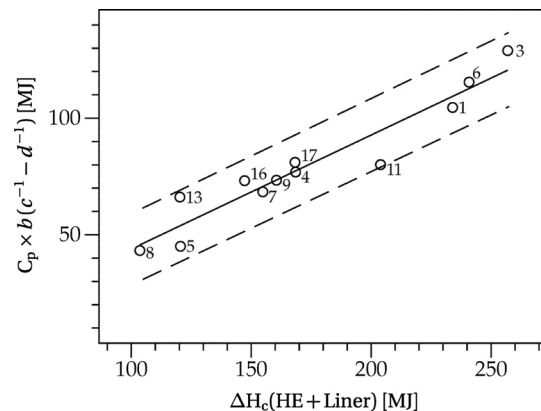
**Fig. 4** Scatter plot between empirical model-predicted initial temperature and initial temperature predicted from thermodynamic properties. Lack of correlation suggests initial temperature is not a good variable for event classification.

Fig. 5, and is the key finding in the present study. The relationship of Eq. (2) is well supported by the experimental results and offers a potential event classification discriminator. By observing the effect of secondary combustion on the temperature decay profile, information related to the combustion heat release may be discerned. A linear fit to the data of Fig. 5 provides a slope of  $0.49 \pm 0.1$ , suggesting only half of the available energy is released in the fireball or convective cooling rates are comparable with the combustion rates. Note that errors in the absolute temperature estimation would lead to a different fraction of the combustion heat realized. However, convective cooling obscures this

**Fig. 5** Correlation between predicted and observed heats of combustion with slope of  $0.49 \pm 0.1$  and correlation coefficient of  $r = 0.96$ .

fraction, and only the scaling of the combustion heat with temperature rise is required for the classification scheme.

The liners exhibit a high heat of combustion. Figure 6 demonstrates that the model-predicted heat of combustion increases as RDX is substituted for increased liner size and may contribute to the temperature rise. This positive slope and its corresponding correlation,  $r = 0.93$ , suggest that perhaps the late-time energy release of the aluminum particles, coming mostly from the liner, is being realized. This notion is supported by the finding that the molar specific heat of combustion for the PE-Al liner is 1.3 to 1.4 times greater than the molar specific heat for RDX.

The efficiency of converting the heat of detonation into driving the explosive expansion of the shock front was



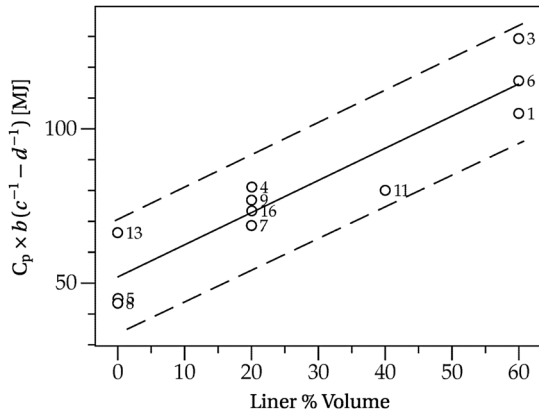


**Fig. 6** Dependence of observed heat of combustion on fraction of volume allocated to the liner, indicating correlation of  $r = 0.93$ .

recently analyzed<sup>29,30</sup> for the present events using the Sedov–Taylor model.<sup>40,41</sup> The results are best described by a constant rate of energy release and near-spherical expansion. The time scale for release of the detonation energy relative to the ideal RDX detonation wave velocity provides a measure of detonation efficiency.

The observed efficiency ranges from 2% to 15% when liner or aluminum is substituted for RDX for those events with blast dimensionalities slightly less than spherical geometry. Efficiencies are less than those typically found in the literature. One might expect the energy not converted to shock expansion to be available for secondary combustion, increasing the temperature of the subsequent fireball. However, there was no significant relationship found between the combustion fit parameters expressed in Eq. (2),  $b(1/c - 1/d)$ , with shock efficiency. Apparently, the heat of detonation not converted to shock is not available for secondary combustion.

### 3.3 Fireball Rise

A study by Kansa concludes that the fireball rise depends upon the mass and initial temperature of the explosion, atmospheric and explosion-generated turbulence, and the fireball's Richardson number.<sup>42</sup> Spatially integrating the fireball's mass, momenta, and total energy differential equations, he models the rise of TNT explosion fireballs from initiation to hundreds of meters in height. The main thrust of his efforts is the long-duration rise profile of an explosion “puff” or what is referred to as the postdetonation particulate cloud (PDPC) in the present work. His analytical expression for buoyant velocity assumes the PDPC mass, density difference, dimensions, lateral and rise speeds, and turbulence parameters as slowly varying quantities. Unfortunately, these assumptions are not applicable at the early times of an explosion. He explains the eventual elliptical shape of the PDPC as arising from the hot gas imparting a vertical component of momentum to the existing radial momentum and thus distorting the initial spherical shape into a mushroom-shaped cloud. During his model development, he also expresses the vertical speed of the top boundary of the rising PDPC as<sup>42</sup>

$$s_z^\pm = -\left(\frac{h^\pm}{r}\right) \frac{dr}{dt} \quad (9)$$

where  $h^\pm$  is the height of PDPC top (+) and bottom (–), and  $r$  is the radius of the rising PDPC.

We have recently characterized the rate of PDPC lofting from high-speed visible imagery.<sup>29,30</sup> A summary of these rates for each of the current events is included in Table 4. The resulting vertical speeds at the PDPC top,  $s_z^+$ , have variances too large to provide meaningful insights into the PDPC rise phenomenon using this simplified relation for the test articles in the present work.

As an alternative approach, we examine Kansa's assertion on the temperature dependence of the PDPC rise. The observed lofting rates are correlated with the present results for fireball initial temperature,  $T_o$ , and the combustion fit parameters representation of temperature,  $b(1/c - 1/d)$ , in Fig. 7. The combustion fit parameters and the fireball rise have a significant correlation coefficient of  $r = 0.75$ . When  $T_o$  is correlated to PDPC rise, two outlier events (E5 and E9) are readily identified. If the two outlier events are excluded, the  $T_o$  and fireball rise are well correlated to within 94% and are consistent with Kansa's assertion. With the outliers included, the correlation is not significant at  $r = 0.33$ . Turbulence and atmospheric stability influence the rise height. However, the dataset is too sparse, and the variance in recorded wind speeds at the test site is too great for a definitive investigation.

Weil et al.<sup>43,44</sup> and Bjorklund et al.<sup>45</sup> have also examined plume rise during their development of open-burn and open-detonation dispersion models for environmental impact studies. Although also primarily aimed at long-duration plume and cloud rise occurring over hundreds of meters, their model attempts to address earlier time plume rise. Weil et al. express the initial cloud rise,  $\Delta h$ , as related to its initial momentum,  $M$ , and buoyancy,  $F$ , using the expression<sup>43</sup>

$$\Delta h = 2.35(Mt + Ft^2)^{1/4}, \quad (10)$$

where

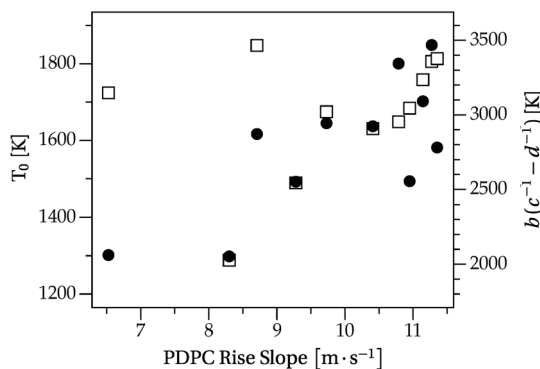
$$M = \frac{4\pi}{3} r_o^2 w_o$$

$$F = \frac{gQ}{c_p \rho \theta}.$$

They define  $w_o$ ,  $r_o$ , and  $Q$  as the initial velocity, radius, and heat content of the cloud, respectively. The variables  $g$ ,  $c_p$ ,  $\rho$ , and  $\theta$  represent the gravitational acceleration, specific heat of the air, ambient air density, and potential temperature, respectively. To compare the above model to the data in the present work, extracted radius and observed PDPC loft rate as well as heat of combustion and a fireball temperature of 1300 K for data PDPC loft heights above 10 m were inputted into Eq. (2). For several events tested, there was a 10% to 30% difference between the data and the model-predicted cloud rise height within the first 0.5 s after detonation. Equation (2) appears more sensitive to PDPC radius and velocity and less so to heat content or PDPC temperature. Given the physical complexity of a rising fireball, finding a precise model to describe the lofting rate proved difficult. Nevertheless, a 75% correlation between empirical model fit parameter-derived temperature and PDPC rise suggests

**Table 4** Comparison of fit parameters to thermodynamic predictions.

Event	Detonation	Combustion			PDPC
	$\Delta H_{d,HE}/C_{p,d}$ (K)	$(A\sigma_{SB})/C_{p,c}$ ( $\times 10^{-10}$ s $^{-1}$ K $^{-3}$ )	$\Delta H_c/C_{p,c}$ (K)	b ( $l/c - 1/d$ ) (K)	Rise slope (m/s)
E8	4363.87	8.96	4924.78	2054.77	8.29 $\pm$ 0.54
E13	4284.43	8.78	5594.49	3089.38	11.58 $\pm$ 1.14
E5	4320.79	8.63	5510.63	2062.52	7.18 $\pm$ 0.78
E16	3748.88	7.54	5881.30	2924.79	10.40 $\pm$ 0.51
E7	3624.51	7.01	5749.57	2551.03	9.27 $\pm$ 0.38
E9	3684.64	7.36	6258.36	2871.18	8.16 $\pm$ 1.04
E4	3561.06	6.83	6101.00	2781.39	11.01 $\pm$ 0.49
E17	3558.57	6.85	6102.46	2942.47	9.66 $\pm$ 0.75
E11	2880.83	6.02	6505.47	2556.62	11.03 $\pm$ 0.79
E1	2207.68	5.73	7096.70	3179.21	none
E6	2136.14	5.67	7229.97	3469.56	10.81 $\pm$ 1.30
E3	1963.90	4.89	6644.54	3344.32	10.78 $\pm$ 0.97

**Fig. 7** Relationship between lofting rate and ( $\square$ )  $T_0$  and ( $\bullet$ ) combustion fit parameters.

a possible relationship between buoyant fireball rise and temperature.

#### 4 Conclusions

We have identified an effective, temporally integrated temperature, in excess of the radiatively cooled initial temperature, during the secondary combustion of detonation fireballs as strongly correlated with event's heat of combustion. Event classification based on hydrogen-to-carbon ratios as previously developed from the CO, CO<sub>2</sub>, and H<sub>2</sub>O spectral features may be augmented by the observed temperature dynamics to reveal information regarding heat of combustion and thus the weight of the explosive material.

Two spectral bands, 2500 to 2700 cm<sup>-1</sup> and 4500 to 4700 cm<sup>-1</sup>, have been identified to estimate the evolving fireball temperature. The temperatures agree well with a simple radiative transfer model and decay from initial values of ~1300 to 1850 K to about 1000 K over a 1-s interval. Secondary maxima are observed in the evolution of the fireball temperatures and are related to the available heat of combustion. Indeed a strong correlation exists between the empirical model's estimate of the heat of combustion and the thermodynamic properties of the HE (RDX and aluminum) and liner. Test articles with higher aluminum and liner content exhibit higher fireball temperatures over an extended interval. Approximately 50% of the available energy is partitioned to the gaseous fireball. Furthermore, the empirical heat released increases linearly with the fraction of the volume allocated to the liner.

The increased understanding of remote optical signatures from detonation fireballs suggests possible information for classification of event type. The instrumentation is insufficient to observe the initial fireball temperature, and peak temperatures exhibit no significant correlation with the heat of detonation. Even with a very fast spectrometer, the efficiency of high-explosive detonation may be highly variable for similar events. However, the relative temporal dynamics of the temperature profiles do appear useful for classification. If an estimate for the heat of detonation could be determined, possibly from the shock dynamics, then the empirical value for the heat of combustion might specify the relative partitioning between high-explosive content and aluminum or liner fraction. The present data sample a small selection of high-explosive compositions with minimal repeatability in event type. Further investigation is

required to develop a complete set of key features for classification and to evaluate the probability distribution functions for various event classes.

## References

1. A. N. Dills, G. P. Perram, and S. C. Gustafson, "Detonation discrimination techniques using a near-infrared focal plane array camera," *Proc. SPIE* **5431**, 77–86 (2004).
2. K. C. Gross, "Phenomenological model for infrared emissions from high-explosive detonation fireballs," Ph.D. Dissertation, AFIT/DS/ENP/05-01, Department of Physics, Air Force Institute of Technology (2005).
3. K. C. Gross, A.N. Dills, and G.P. Perram, "Phenomenology of exploding ordnance using spectrally and temporally resolved infrared emissions," *Proc. SPIE* **5075**, 217–227 (2003).
4. K.C. Gross and G.P. Perram, "The phenomenology of high explosive fireballs from fielded spectroscopic and imaging sensors for event classification" *Int. J. High Speed Electron. Syst.* **18**(1), 19–29 (2008).
5. K.C. Gross, G.P. Perram, and R.F. Tuttle, "Modeling infrared spectral intensity data from bomb detonations," *Proc. SPIE* **5811**, 100–111 (2005).
6. K.C. Gross, J. Wayman, and G.P. Perram, "Phenomenological fireball model for remote identification of high-explosives," *Proc. SPIE* **6566**, 656613 (2007).
7. J.A. Orson, W.F. Bagby, and G.P. Perram, "Infrared signatures from bomb detonations," *Infrared Phys. Technol.* **44**(2), 101–107 (2003).
8. J. Wilkinson et al., *Shock Compression of Condensed Matter* **955**(1), 1271–1274 (2007).
9. J. R. Carney et al., "Time-resolved optical measurements of the post-detonation combustion of aluminized explosives," *Rev. Sci. Instrum.* **77**(6), 063103 (2006).
10. M. A. Cook et al., "Aluminized explosives," *J. Phys. Chem.* **61**(2), 189–196 (1957).
11. I. Glassman, "Metal combustion processes," AFOSR T.N. No. 59-1093, AD 228566, Aeronautical Engineering Laboratory Report No. 473, Princeton University (1959).
12. T. A. Brzustowski and I. Glassman, "Spectroscopic investigation of metal combustion," ADA 952023, Aeronautical Engineering Laboratory Report No. 586, Princeton University (1961).
13. D. Price, A. R. Clairmont, and J. O. Erkman, "Explosive behavior of aluminized ammonium perchlorate," Naval Ordnance Laboratory Technical Report 72-15, AD 745344 (1972).
14. P. Brousseau et al., "Detonation properties of explosives containing nanometric aluminum powder," in *Int. Detonation Symposium*, San Diego, California (2002).
15. A. Lefrancois et al., "Nanometric aluminum powder influence on the detonation efficiency of explosives," in *Int. Detonation Symposium*, San Diego, California (2002).
16. P. E. DesJardin, J. D. Felske, and M. D. Carrara, "Mechanistic model for aluminum particle ignition and combustion in air," *J. Propul. Power* **21**(3), 478–485 (2005).
17. F. Zhang and K. Gerrard, "Reaction mechanism of aluminum-particle-air detonation," *J. Propul. Power* **25**(4), 845–858 (2009).
18. E. L. Baker et al., "Combined effects of aluminized explosives," Technical Report ARMET-TR-10007, AD-E403299, U. S. Army ARDEC (2010).
19. J. R. Carney et al., "Atmospheric effects on the combustion of detonating aluminized explosives," *Shock Compress. Cond. Matt.* **845**(1), 948–951 (2006).
20. W. F. Bagby, "Spectral and temporal characterization of high-temperature events," M. S. Thesis, AFIT/GAP/ENP/01M-01, Department of Engineering Physics, Air Force Institute of Technology (2001).
21. K.C. Herr, D.K. Stone, and D.S. Urevig, "Infrared spectroscopy of high explosive detonations: the Sandia experiments," Report No. ATR-82 (7953)-1, Aerospace Corporation (1982).
22. J. A. Orson, "Collection of detonation signatures and characterization of spectral features," M. S. Thesis, AFIT/GSO/ENP/00M-01, Department of Engineering Physics, Air Force Institute of Technology (2000).
23. M. F. Gogulya, A. Y. Dolgoborodov, and M. A. Brazhnikov, "Investigation of shock and detonation waves by optical pyrometry," *Int. J. Impact Eng.* **23**(1), 283–293 (1999).
24. W.K. Lewis and C.G. Rumschik, "Measurement of apparent temperature in post-detonation fireballs using atomic emission spectroscopy," *J. Appl. Phys.* **105**(5), 056104 (2009).
25. T. Ogura et al., "Pyrometry study on fireballs generated upon the explosion of TNT," in *34th Int. Annual Conf. ICT*, Vol. 18, pp. 1–12, Fraunhofer Institute for Chemical Technology Karlsruhe, Germany (2003).
26. S. Goroshin et al., "Optical pyrometry of fireballs of metalized explosives," *Propell. Explos. Pyrotech.* **31**(1), 1–13 (2006).
27. K. C. Gross et al., "Simulating systematic scene-change artifacts in Fourier-transform spectroscopy," *Proc. SPIE* **7695**, 76951Y (2010).
28. J.M. Gordon, K.C. Gross, and G.P. Perram, "Temporally-resolved, infrared spectra from the detonation of advanced munitions," *Proc. SPIE* **7330**, 733006 (2009).
29. J. M. Gordon, K.C. Gross, and G.P. Perram, "Fireball and shock wave dynamics from the detonation of aluminized novel munitions," *Combust. Explos. Shock Waves* **49**(4), 450–462 (2013).
30. J. M. Gordon, "Shock wave dynamics of novel aluminized detonations and empirical model for temperature evolution from post-detonation combustion fireballs," Ph.D. Dissertation, AFIT/DS/ENP/10-S03, Department of Physics, Air Force Institute of Technology (2010).
31. P. W. Cooper, *Explosives Engineering*, VCH Publishing, New York (1996).
32. M. W. Chase, Jr., Ed., *NIST-JANAF Thermochemical Tables*, 4th ed., American Chemical Society, Woodbury, New York (1998).
33. H. E. Revercomb et al., "Radiometric calibration of IR Fourier transform spectrometers: solution to a problem with the high-resolution interferometer sounder," *Appl. Opt.* **27**(15), 3210–3218 (1988).
34. L.S. Rothman et al., "The high resolution transmission (HITRAN) molecular spectroscopic database and HAWKS (HITRAN Atmospheric Workstation): 1996 edition," *J. Quant. Spect. Rad. Trans.* **60**(5), 665–710 (1998).
35. M. F. Modest, *Radiative Heat Transfer*, 2nd ed., Academic Press, Burlington, Massachusetts (2003).
36. H. Chang and T.T. Charalampopoulos, "Determination of the wavelength dependence of refractive indices of flame soot," *Proc. R. Soc. Ser. A* **430**, 577–591 (1990).
37. J. T. Yardley, *Introduction to Molecular Energy Transfer*, Academic Press, New York (1980).
38. W. Lee, I.V. Adamovich, and W.R. Lampert, "Optical pumping studies of vibrational energy transfer in high-pressure diatomic gases," *J. Chem. Phys.* **114**(3), 1178–1186 (2001).
39. B. J. Steward, K. C. Gross, and G. P. Perram, "Modeling midwave infrared muzzle flash spectra from unsuppressed and flash-suppressed large caliber munitions," *Infrared Phys. Technol.* **55**(4), 246–255 (2012).
40. L. I. Sedov, "Asymptotic Laws of Shock Wave Decay," in *Similarity and Dimensional Methods in Mechanics*, M. Holt, Ed., 4th ed., Academic Press, New York (1959).
41. G. I. Taylor, "The formation of a blast wave by a very intense explosion. I. Theoretical discussion," *Proc. R. Soc. A* **201**, 159–174 (1950).
42. E. J. Kansa, "A time-dependent buoyant puff model for explosive sources," Report No. UCRL-ID-128733 Rev. 1, Lawrence Livermore National Laboratory (1997).
43. J.C. Weil et al., "Dispersion model development for open burn/open detonation sources," in *9th Joint Conf. Applications of Air Pollution Meteorology*, American Meteorological Society, Boston, Massachusetts (1996).
44. J.C. Weil, B. Templeman, and W. Mitchell, "Progress in developing an open burn/open detonation dispersion model," Air and Waste Management Assoc., Pittsburgh, Pennsylvania (1996).
45. J.R. Bjorklund et al., "Open burn/open detonation dispersion model (OBODM) user's guide volume II. Technical description," DPG Document No. DPG-TR-96-008b, U.S. Army Dugway Proving Grounds (1998).

**J. Motos Gordon** graduated from the Air Force Institute of Technology (AFIT) with a PhD degree in physics in 2011. He is a lieutenant colonel in the United States Air Force with a recent assignment at the Defense Threat Reduction Agency.

**Kevin C. Gross** graduated from the Air Force Institute of Technology (AFIT) with a PhD degree in physics in 2007. He joined the AFIT faculty in 2008 and currently is an assistant professor. He runs the AFIT Remote Sensing Group and has been involved in the collection of high-speed radiometric, imagery, and spectroscopic measurement of battle space combustion signatures including high-explosive detonations, muzzle flashes, rocket engines, and jet engine exhaust plumes.

**Glen P. Perram** received his BS degree from Cornell University in 1980 and his MS and PhD degrees from the Air Force Institute of Technology (AFIT) in 1981 and 1986, respectively. As professor of physics at AFIT, his research interests include high-power gas lasers, remote sensing, and laser-material interactions.